Journal of Alloys and Compounds 590 (2014) 324–330

(doi: 10.1016/j.jallcom.2013.12.120)

http://dx.doi.org/10.1016/j.jallcom.2013.12.120

Synthesis, phase evolution and properties of phase-pure nanocrystalline $BiFeO_3$ prepared by a starch-based combustion method

Roberto Köferstein

Institute of Chemistry, Inorganic Chemistry, Martin-Luther-University Halle-Wittenberg, Kurt-Mothes-Strasse 2, 06120 Halle, Germany.

Tel.: +49-345-5525630; Fax: +49-345-5527028.

E-mail address: roberto.koeferstein@chemie.uni-halle.de

Abstract. The preparation of phase-pure nano-sized $BiFeO_3$ by a combustion-like method using starch as complexing agent is described herein. Phase evolution and development of the crystallite size during the synthesis were monitored depending on the heat treatment and the composition of the (BiFe)-gels. Phase-pure $BiFeO_3$ was obtained at a low heating rate and calcination temperatures between 500 and 600 °C. Above 600 °C the $BiFeO_3$ gradually decomposed to $Bi_{25}FeO_{40}$ and $Bi_2Fe_4O_9$. The investigations showed that the appearance of secondary phases depends on the heating rate, calcination temperature, and the fuel to oxidizer ratio in the (BiFe)-gel. The use of HNO_3 instead of acetic acid in the preparation of

the (BiFe)-gel promotes the formation of secondary phases. To study the phase stability the phase-pure $BiFeO_3$ powder (**1c**) obtained after calcining at 550 °C (d_{cryst} = 37 nm) was sintered to ceramic bodies up to 800 °C. During sintering the $BiFeO_3$ phase decomposed to $Bi_{25}FeO_{40}$ and $Bi_2Fe_4O_9$ gradually. The activation energy for the decomposition process during sintering was calculated to 337±19 kJ/mol using the *Johnson–Mehl–Avrami–Kolmogorov* (JMAK) model. Magnetic measurements on phase-pure $BiFeO_3$ powders show maximal magnetization of about 0.7 emu/g at 90 kOe and coercivities between 5−7 kOe at 300 K. Investigations at 10 K reveal a loop shift (exchange-bias) up to 2.9 kOe in the negative direction. The optical band gaps of the phase-pure $BiFeO_3$ powders were determined as 2.28(4) eV.

Keywords: *Bismuth orthoferrite; perovskite; ceramic; magnetism; phase stability, band gap*

1. Introduction

The perovskite-related bismuth orthoferrite ($BiFeO_3$) is of interest because of its high potential for advanced technologies. $BiFeO_3$ has been investigated for application as capacitors, nonvolatile memory, and magnetoelectric devices [1−4]. Photocatalytic activities of $BiFeO_3$ have also been reported [5,6]. *Alexe* and *Hesse* [7] described an abnormal photovoltaic effect in bulk $BiFeO_3$. Bismuth orthoferrite as photoelectrode material for water splitting was tested by *Chen* et al. [8]. Moreover, $BiFeO_3$ can act as a heterogeneous catalyst in both Fenton-like reactions during the wet peroxide oxidation of hydrocarbons [9] and in acetylation processes of amines, phenols and alcohols [10].

Bulk $BiFeO_3$ is G-type antiferromagnetic material with a spiral spin structure (period length of 62 nm) [11]. $BiFeO_3$ crystallizes in a rhombohedrally distorted perovskite structure (space group R3c), has a ferroelectric *Curie* temperature of $T_c \approx 830$ °C and an antiferromagnetic

Néel temperature of $T_N \approx 370$ °C [12]. *Arnold* et al. [13] found out that at the *Curie* temperature $BiFeO_3$ undergoes a ferroelectric first order transition to the orthorhombic space group Pbnm.

Apart from the classical mixed-oxide method some wet-chemical syntheses have been developed to obtain nano-sized or fine-grained $BiFeO_3$ powders [5,6,14–24]. Closer inspection shows that many synthesis routes lead to $BiFeO_3$ powders with small amounts of secondary phases, such as $Bi_{25}FeO_{40}$, $Bi_2Fe_4O_9$ and Bi_2O_3 [9,10,17,23,25–37]. The $Bi_{25}FeO_{40}$ phase is also written as $Bi_{25}FeO_{39}$ [38,39]. Such impurities can be removed by treatment with dilute HNO_3 [31–36]. However, due to the formation of these Bi- or Fe-rich phases and their leaching out with HNO_3 the remaining $BiFeO_3$ phase can possess Bi or Fe vacancies [23]. $BiFeO_3$ is described as a metastable compound which partial decomposes to $Bi_{25}FeO_{40}$ and $Bi_2Fe_4O_9$ [40–42]. The beginning of the decomposition process varies between 500 and 930 °C and depends on several parameters such as preparation method, heat treatment, and particle sizes [43–45].

As described earlier, nano-sized particles can be obtained in a combustion-like process [46,47].

The aim of this paper is to describe a new, simple, and fast synthesis route to obtain phase-pure and nano-sized $BiFeO_3$ powders in which starch acts as a complexation agent and gellant, because starch is an eco-friendly and cheap abundant biopolymer. The phase evolution during the calcination process was monitored by XRD and thermal analysis. The appearance of secondary phases was studied with respect to the thermal treatment and the compositions of the starting (BiFe)-gels. The phase stability and kinetics of decomposition of the obtained nanocrystalline $BiFeO_3$ powders during sintering were investigated using the *Johnson–Mehl–Avrami–Kolmogorov* (JMAK) model. Additionally, the magnetic behaviour and the optical band gap were studied.

2. Experimental

2.1. Material preparation

Synthesis **I**: $Bi(NO_3)_3 \cdot 5H_2O$ (0.006 mol, *Merck*) was dissolved in 2 g acetic acid (≥99.8 % Sigma-Aldrich) and 5 ml deionized water. $Fe(NO_3)_3 \cdot 9H_2O$ (0.006 mol, *Merck*) was added together with further 5 ml deionized water. After addition of 6.0 g soluble starch (*Sigma-Aldrich*) the resulting turbid solution was continuously stirred (if applicable heating to about 35 °C) until it became a high viscous gel, abbreviated as (BiFe)-gel-**I** in the following.

Syntheses **IA** refers to a modified synthesis route using 1.2 g soluble starch resulting in (BiFe)-gel-**IA**.

Syntheses **II** and **IIA** are analogous to synthesis **I**, however $Bi(NO_3)_3 \cdot 5H_2O$ was dissolved in 1 g HNO_3 (65 %) and 5 ml deionized water. In synthesis **II** 6.0 g starch and in synthesis **IIA** 9.9 g starch were used. The resulting gels are abbreviated as (BiFe)-gel-**II** and (BiFe)-gel-**IIA**.

All (BiFe)-gels were calcined in static air in an Al_2O_3 crucible at various temperatures up to 750 °C yielding different $BiFeO_3$ powders.

To produce ceramic bodies the (BiFe)-gel-**I** was calcined at 550 °C for 1 h with a heating rate of 1 K/min yielding powder **1c**. That powder was pressed into pellets (green density: 3.5 g/cm^3) without using any pressing aid. The pellets were placed on a ZrO_2 fibre mat and sintered to ceramic bodies.

2.2. Characterization

X-ray powder diffraction data were collected at room temperature on a *Bruker D8-Advanced* diffractometer, equipped with a one-dimensional silicon strip detector (LynxEye™) and operating with Cu-K_α radiation. Powder patterns were refined both with the *Rietveld* program FullProf [48] and the profile fitting software PowderCell [49]. Crystallite sizes were

determined from the XRD line broadening using the Scherrer equation and the integral peak breadth (software suite WinXPOW [50]). The Wilson-equation was used to determine the strain parameter [50,51]. Specific surface areas (BET) were determined using nitrogen three-point gas physisorption (Nova 1000, *Quantachrome Corporation*). The equivalent BET particle diameters were calculated assuming a spherical or cubic particle shape. Transmission electron microscopy (TEM) samples were prepared by dispersing the powder in alcohol under ultrasonic agitation and collecting it onto a copper TEM grid covered with a carbon membrane. Scanning electron microscope (SEM) images were recorded with a *Philips* XL30 ESEM (Environmental Scanning Electron Microscope). Diffuse reflectance spectra were obtained at room temperature in the range 380−1000 nm using a *Perkin Elmer* UV−VIS spectrometer Lambda 19 using $BaSO_4$ as a white standard. Magnetic measurements were carried out with a PPMS 9 from *Quantum Design*. Hysteresis loops were taken at 300 K and 10 K with magnetic field cycling between −90 and +90 kOe.

3. Results and discussion

3.1. Powder characterization, TG-DTA and XRD

Heating of the (BiFe)-gel-**I** at 200 °C in air for 0.5 h resulted in a black-brown powder. Simultaneous TG/DTA investigations in flowing air with various heating rates were carried out on this powder. Fig. 1a represents the TG/DTA measurement with a heating rate of 10 K/min. As seen the sample shows a slight weight loss of about 3.0 % up to about 180 °C. Higher temperatures lead to a fast two-step decomposition process. The first step ranges to 345 °C and the following second step is finished up to 535 °C. The DTA curve reveals that the first reaction step is exothermic with an onset temperature of 191 °C and the second reaction step starts at about 315 °C and results in a broad exothermic signal. The exothermic character suggests a combustion-like reaction in which the organic molecules (starch and

acetic acid) act as fuel and the nitrate ions as oxidizing agent. The total weight loss until 535 °C is 70.7 % and up to 750 °C no further significant weight loss can be observed.

TG/DTA measurements with a heating rate of 1 K/min (Fig. 1b) show a weight loss of 4.9 % until 190 °C. Further heating results in a decomposition with a strong weight loss. A first weight loss is finished at 290 °C and the second step caused a total weight loss of 68.3 % up to 390 °C. Two exothermic signals with onset temperatures of 164 and 295 °C can be observed. Until 450 °C there is no significant weight loss. Above 450 °C a last small weight loss to 470 °C can be detected and is probably caused by the decomposition of $Bi_2O_2CO_3$. The total weight loss until 470 °C is 70.6 %.

Fig. 2 shows the phase evolution during the thermal decomposition of the yellow (BiFe)-gel-**I** heated in a muffle furnace in static air at various temperatures with a heating rate of 1 K/min. The starting (BiFe)-gel-**I** (Graph 2a) as well as the calcination product at 300 °C (not shown) are X-ray amorphous. Calcination at 400 °C for 1 h lead to an orange-ochre powder revealing reflections of rhombohedral $BiFeO_3$, $Bi_{24}Fe_2O_{39}$, $Bi_2O_2CO_3$, and Fe_2O_3 [52] (Graph 2b). After heat treatment at 500 °C for 1 h (powder **1a)** reflections of $BiFeO_3$, $Bi_{24}Fe_2O_{39,}$ and $Bi_{25}FeO_{40}$ [52] appear (Graph 2c), whereas rising the calcination time to 5 h phase-pure $BiFeO_3$ (powder **1b**) can be obtained (Graph 2d). Calcinations at 550 and 600 °C for 1 h (heating rate 1 K/min) result in orange-ochre phase-pure rhombohedral $BiFeO_3$ powders **1c** and **1f**, respectively (Graph 2e,f). The XRD pattern of **1c** was refined on the basis of a rhombohedral unit cell (space group: R3c, No. 161) according to ref. [53]. The hexagonal cell metric was calculated as a = b = 558.19(1) pm, c = 1386.04(2) pm, and V = 374.00(1)·10^6 pm^3 in good agreement with reported data [27,53]. The $BiFeO_3$ powder **1c** (550 °C, 1 h) has a specific surface area of 9.3 m^2/g. The volume-weighted average crystallite size (*Scherrer* equation) was calculated as 37 nm. The root-mean-square-strain parameter was obtained according to the Wilson-equation [51] and was found to be 0.002. TEM investigations reveal particles mostly in the range 30–50 nm, with maximum sizes up to 70 nm (Fig. 3). As shown in Tab. 1 the crystallite size

of the $BiFeO_3$ phase rises with increasing calcination temperature up to 243 nm at 750 °C. Higher calcination temperatures of 650 and 750 °C (soaking time 1 h) leads to a partial decomposition of $BiFeO_3$ and the colour of these powders (**1g**, **1h**) progressively turns to brown. Besides $BiFeO_3$ the XRD patterns show $Bi_{25}FeO_{40}$, $Bi_2Fe_4O_9$, traces of monoclinic Bi_2O_3, and $Bi_{24}Fe_2O_{39}$ as secondary phases [52] (Graph 2g,h). Quantitative phase analyses shows that after calcination at 650 °C the amount of secondary phases is about 5 wt.% and at 750 °C the amount rises to 38 wt.%. Table 1 summarizes the phase composition of selected powders. Recently, *Liu* et al. [43] reported on a phase-pure nano-sized $BiFeO_3$, prepared by a co-precipitation method, which decomposed even above 500° C. Thus the powders reported here have a significant higher stability.

Fig. 4 represents the influence of both the heating rate and the annealing time at a calcination temperature of 550 °C for the (BiFe)-gel-**I**. The XRD pattern after calcination at 550 °C for 4 h (heating rate 1 K/min) shows only reflections of $BiFeO_3$ (Graph 4a). Whereas an annealing time of at least 5 h leads to secondary phases (8 wt.%) such as $Bi_{25}FeO_{40}$ and $Bi_2Fe_4O_9$ (powder **1d)** as shown in graph 4b and Tab. 1. *Carvalho* and *Tavares* [54] and *Morozov* et al. [55] also found a decomposition of $BiFeO_3$ after prolonged annealing time. Decomposition of the (BiFe)-gel-**I** at 550 °C for 1 h with a heating rate of 10 K/min results in the formation of $BiFeO_3$ and small amounts (13 wt.%) of $Bi_2Fe_4O_9$, $Bi_{25}FeO_{40}$ and $Bi_{24}Fe_2O_{39}$ (powder **1e**, Graph 4c) in contrast to the calcination process with 1 K/min (see Tab. 1). Analogous results were obtained for a calcination temperature of 600 °C. *Hardy* et al. [24] also reported that high heating rates lead to the formation of secondary phases.

The formation of secondary phases is additionally influenced by the composition of the starting (BiFe)-gel. As mentioned above, during the calcination of the (BiFe)-gel-**I** starch and acetic acid act as fuel and the nitrate ions as oxidizer. As reported by *Deraz* [56] the fuel to oxidizer ratio influences the formation of secondary phases during combustion-like processes. During the oxidation of the organic molecules (starch and acetic acid) only the element

carbon changes its oxidation number. Therefore, in the following consideration the carbon to nitrate ratio (C/N) will be used. (BiFe)-gel-**I** has a C/N ratio of 8.0 and lead to the formation of phase-pure $BiFeO_3$ at 550 °C (powder **1c**). In contrast a C/N ratio of 1.25 in (BiFe)-gel-**IA** leads to the formation of $BiFeO_3$ and traces of secondary phases (2 wt.%) after calcination at 550 °C for 1 h (heating rate 1 K/min) (powder **2**, Fig. 5a). Additionally, a reduction of the C/N ratio causes slightly increasing crystallite sizes of the $BiFeO_3$ phase (Tab. 1). Preparing of the (BiFe)-gel-**II** (C/N = 4.8) using HNO_3 instead of acetic acid and following calcination at 550 °C for 1 h (heating rate 1 K/min) results in the appearance of both $Bi_2Fe_4O_9$ and $Bi_{25}FeO_{40}$ besides $BiFeO_3$ (powder **3**, Graph 5b). The amount of secondary phases was calculated as 16 wt.% (Tab. 1). As pointed out by *Hwang* and *Wu* [57] and *Deshpande* et al. [58] the maximum combustion temperature (T_c^{max}) is correlated with the fuel/oxidizer ratio. Increasing fuel/oxidizer (C/N) ratios from fuel lean to stoichiometric amounts leads to raising T_c^{max} values. However, very high C/N ratios (fuel rich) causes a decrease of T_c^{max}, because of the high amount of gases released which dissipates heat [59]. Therefore, (BiFe)-gels with lower C/N ratios may lead to higher T_c^{max}, which promotes secondary phases as mentioned above. The slightly larger crystallite sizes for samples with lower C/N ratios indicate higher T_c^{max} values, as seen in Tab. 1.

Moreover, the appearance of secondary phases when HNO_3 is used is not only caused by a lower C/N ratio, because a C/N ratio of 8.0 ((BiFe)-gel-**IIA**) leads to the formation of Bi- and Fe-rich phases (powder **4**, Graph 5c). However, the amount of these phases in powder **4** is slightly smaller (11 wt.%) than in powder **3** (Tab. 1). The reason for that finding might be that the dissolving of $Bi(NO)_3$ in an aqueous acetic acid solution leads to a more stable complexation between the acetic anion and the metal cation than in an aqueous HNO_3 solution. It can be supposed that the more stable complexation with the acetic anion inhibit

the selective precipitation of Bi- and Fe-species during the calcination process, resulting in a homogeneous bismuth–iron distribution.

As a result the formation of phase-pure $BiFeO_3$ depends not only on the calcination parameters, but also on the fuel/oxidizer ratio and on the conditions for preparing a stable bismuth nitrate solution and thus a stable (BiFe)-gel.

3.2. Phase stability and densification during sintering

To obtain ceramic bodies of $BiFeO_3$ or materials based on $BiFeO_3$ the conventional (isothermal) sintering process is widely-used [27,60,61]. Because of the low stability of nano $BiFeO_3$ at elevated temperatures, both the kinetics of the decomposition process and the densification during sintering were investigated. Fig. 6a shows the final densities of powder compacts from the nano-sized powder **1c** after isothermal sintering in static air. The bulk densities of the sintered bodies were calculated from their weight and geometric dimensions. The relative densities were related to the crystallographic density of 8.31 g/cm^3 for rhombohedral $BiFeO_3$ [62]. Conventional sintering (heating up with a rate of 10 K/min, soaking for 1 h and cooling down with 20 K/min) at temperatures between 550 and 800 °C resulted in ceramic bodies with relative densities up to 78 % (6.50 g/cm^3). As seen in Fig. 6b conventional sintering of phase-pure powder compacts of **1c** results in a partial decomposition of $BiFeO_3$ to $Bi_2Fe_4O_9$ and $Bi_{25}FeO_{40}$ with raising temperature. To describe the kinetics of the decomposition process of $BiFeO_3$ compacts during conventional sintering up to 800 °C the widely-used *Johnson–Mehl–Avrami–Kolmogorov* (JMAK) model was used (Eq. 1) [63,64]:

$$\ln[-\ln(1-\alpha] = n \cdot \ln k + n \ln t \quad (1)$$

where α is the fraction of the decomposed $BiFeO_3$, n the *Avrami* exponent, k the rate parameter and t the annealing time. k and n can be calculated from a plot of $\ln[-\ln(1-\alpha)]$

versus ln*t*. The *Arrhenius* equation combined the rate constant *k* with the activation energy (Eq. 2):

$$\ln k = \ln A - \frac{E_A}{RT} \quad (2)$$

where *A* is a pre-exponential factor, E_A the activation energy, *R* the universal gas constant and *T* the absolute temperature. E_A can be determined from the slope of ln*k* versus 1/*T* (Fig. 7). The activation energy for the decomposition of $BiFeO_3$ during conventional sintering was calculated as E_A = 337(19) kJ/mol.

To reduce the decomposition of nano-$BiFeO_3$ lower sintering temperatures are required. Both lower sintering temperatures and an improvement of the densification can be achieved applying a 2-step sintering process [65] as shown in the inset of Fig. 6a. For that purpose, powder compacts of **1c** were fast heated (30 K/min) to a higher temperature (T_1), then cooled (30 K/min) and held at a lower temperature (T_2). The first sample was sintered with T_1 = 770 °C, T_2 = 650 °C and a soaking time of 1 h. The ceramic has a relative density of 69 % (5.71 g/cm^3) and the fraction of secondary phases accounts to 19 wt.%. A second sample sintered at T_1 = 800 °C, T_2 = 550 °C and a soaking time of 3 h achieved a relative density of 80 % (6.63 g/cm^3) and the secondary phases increased to 31 wt.%. (Fig. 6). Compared to the conventional sintering the 2-step sintering process leads to ceramic bodies with higher density and to a lower decomposition of $BiFeO_3$. As seen in Fig. 6 conventional sintering to a relative density of 69 and 80 % results in a strong decomposition of $BiFeO_3$ with fractions of secondary phases of > 60 wt.% and 97 wt.%, respectively. *Wang* et al. [66] reported on a rapid reaction sintering process between Bi_2O_3 and Fe_2O_3 (liquid phase sintering) with enormous heating rates up to 100 K/s to prevent the formation of secondary phases.

3.3. Magnet measurements

The evolution of the magnetization (M) depending on the applied field (H) at 300 K is demonstrated in Fig. 8a for powders **1b**, **1c**, and **1f**, calcined at 500 °C for 5 h, 550 °C for 1 h, and 600 °C for 1 h, respectively. These phase-pure nano-sized $BiFeO_3$ powders reveal large coercivity values (H_c) ranging from 5 to 7 kOe, whereas the remanences (M_r) are about 0.07 emu/g. The maximal magnetization (M_{max}) at 90 kOe varied between 0.61 and 0.72 emu/g. As mentioned above calcining temperatures above 600 °C lead to samples with increasing amounts of secondary phases and larger crystallite sizes. The broadness of the resulting hysteresis loops show a significant reduction in such away that powder **1h** posses values of H_c = 0.24 kOe, M_r = 0.004 emu/g and M_{max} = 0.50 emu/g.

Magnetic measurements at 10 K (Fig. 8b) show H_c values between 7.3 and 10.9 kOe, remanences of about 0.11 emu/g, and M_{max} between 0.84 and 0.67 emu/g. The hysteresis loops at 10 K reveal different coercivity values for decreasing ($H_{c(df)}$) and increasing field ($H_{c(if)}$) as demonstrated for powder **1c** in the inset in Fig. 8b. This exchange bias-like behaviour results in a significant shift of the M–H loops (ΔH_c) in the negative direction with respect to the origin (H = 0). The coercivity shift is defined as $\Delta H_c = \left| 0.5(H_{c(df)} + H_{c(if)}) \right|$ and shows values of 1.90 kOe (powder **1b**), 1.94 kOe (powder **1c**) and 2.89 kOe (powder **1f**), respectively. ΔH_c decreases for powders **1g** and **1h** (calcined above 600 °C) to 1.25 and 0.063 kOe, respectively, because of the larger crystallite.

Measurements both at 300 K and 10 K show that the magnetization almost linearly increases with the applied field (H) indicating mainly an antiferromagnetic ordering of the spins [67]. Moreover, the formation of hysteresis loops is typical for a weak ferromagnetic characteristic (also called parasitic ferromagnetism [68]) as a result of the canted anti-ferromagnetic spin order of $BiFeO_3$ (G-type) [69]. Additionally, as mentioned above, samples with small crystallite sizes (**1b**, **1c**, **1f**) show pronounced hysteresis loops than samples with larger crystallite sizes (**1g**, **1h**). Since the spins at the surface have a reduced coordination, the anti-

ferromagnetic order is disturbed at the surface. Consequently the spins at the surface are not fully compensated resulting in a weak ferromagnetism. The effect increases with decreasing crystallite sizes (increasing surface-volume ratio). On the other hand, the observed weak ferromagnetism is also caused by the suppression of the spiral spin structure in particles lower than 62 nm [70,71]. The observed exchange bias effect at 10 K is caused by the exchange coupling between the ferromagnetic surface and the anti-ferromagnetic core [71].

3.3. Diffuse reflectance measurements

Fig. 9 shows the diffuse reflectance spectra of the $BiFeO_3$ powders **1b**, **1c** and **1f**, respectively. The *Kubelka–Munk* function (4) [72] was used for analysis of the spectra.

$$F(R) = \frac{\alpha}{s} = \frac{(1-R)^2}{2R} \quad (4)$$

where $F(R)$ is the *Kubelka–Munk* function, R the reflectance, α the absorption coefficient and s is the scattering factor. Since the scattering factor is wavelength independent, $F(R)$ is proportional α [73]. The absorption coefficient α is connected with the band gap energy according to equation 5 [74].

$$\alpha h\nu = k(h\nu - E_g)^{1/n} \quad (5)$$

where k is an energy-independent constant, E_g the optical band gap. The exponent n is determined by the type of transition (n = 2 direct allowed, n = 2/3 direct forbidden, n = 1/2 indirect allowed, n = 1/3 indirect forbidden). The *McLean* analysis [75,76] of the absorption

edge was applied to find the type of transition. As mentioned above $F(R)$ is proportional to α and the exponent n can be determined by plotting $(F(R)\cdot h\nu)^n$ vs. $h\nu$. The best fit to a straight line near the absorption edge was found assuming a direct allowed transition (n = 2) in accordance with reports by *Li* et al. [77], *Basu* et al. [78] and *Catalan* and *Scott* [79]. From a plot of $(F(R)\cdot h\nu)^2$ vs. $h\nu$ (inset in Fig. 9) the optical band gap can be obtained by extrapolating the slope to $F(R) \rightarrow 0$.

The band gap energies for the phase-pure $BiFeO_3$ powders were determined as 2.29(4) eV (powder **1b)**, 2.28(4) eV (powder**1c**), and 2.27(6) eV (powder **1f**). The energies of the optical band gaps do not significantly differ from each other because of the narrow crystallite sizes of 36–41 nm of the powders. The values of the band gaps are comparable with previous literature data [31,77,79].

Conclusion

$BiFeO_3$ powders were synthesized by a combustion-like method using metal-nitrates, acetic acid, and starch as complexing reagent and gellant. Calcination of the resulting (BiFe)-gel with a heating of 1K/min between 500 to 600 °C leads to phase-pure nano-sized $BiFeO_3$ powders. Calcination at 550 °C for 1 h leads to powder **1c** with S_{BET} = 9.3 m^2/g and a crystallite size of about 37 nm. TEM images show particles mainly in the range of 30–50 nm. Prolonged heat treatment as well as calcination above 600 °C leads to the formation of secondary phases. The evolution of secondary phases also depends on the fuel/oxidizer ratio as well as on the heating rate. Additionally, phase-pure samples were only obtained using acetic acid (instead of HNO_3) for preparing a stable bismuth iron gel. The decomposition of nano $BiFeO_3$ to $Bi_2Fe_4O_9$ and $Bi_{25}FeO_{40}$ was investigated during sintering of compacts from powder **1c**. The kinetics of the decomposition process reveals an activation energy of 337(19)

kJ/mol using the *JMAK* model. Magnetic measurements of the phase-pure $BiFeO_3$ powders show a behaviour typical for a canted antiferromagnetic material. At 300 K maximal magnetizations at 90 kOe of about 0.7 emu/g were found. The observed hysteresis loops (H_c = 5−7 kOe) indicating a weak ferromagnetic characteristic. Measurements at 10 K reveals an exchange-bias-like behaviour of the hysteresis curves resulting in a shift of the coercivities of ΔH_c = 1.9−2.9 kOe towards negative field. The optical band gap (direct allow transition) of the nanocrystalline phase-pure $BiFeO_3$ powders was determined as 2.28(4) eV.

Acknowledgements

The author thanks Dr. T. Müller for TG/DTA measurements and Prof. Dr. D. Hesse (Max Planck Institute of Microstructure Physics, Halle/Saale) for the TEM. I am also grateful to Prof. Dr. S.G. Ebbinghaus for reading the manuscript and his helpful discussion. Financial support by the German Science Foundation within the Collaborative Research Centre (SFB 762) “Functionality of Oxide Interfaces” is gratefully acknowledged.

Tab. **1**: Preparation conditions, phase compositions and crystallite sizes for selected $BiFeO_3$ samples

Powder	Synthese (gel)	C/N[1)]	Calcination procedure	Composition[2)]	d_{cryst} (nm)[3)]
1a	(BiFe)-gel-**I**	8.0 [4)]	1 K/min, 500 °C, 1 h	BF + SP (9 wt.%)	–
1b	(BiFe)-gel-**I**	8.0 [4)]	1 K/min, 500 °C, 5 h	BF	36
1c	(BiFe)-gel-**I**	8.0 [4)]	1 K/min, 550 °C, 1 h	BF	37
1d	(BiFe)-gel-**I**	8.0 [4)]	1 K/min, 550 °C, 5 h	BF + SP (8 wt.%)	–
1e	(BiFe)-gel-**I**	8.0 [4)]	10 K/min, 550 °C, 1 h	BF + SP (13 wt.%)	–
1f	(BiFe)-gel-**I**	8.0 [4)]	1 K/min, 600 °C, 1 h	BF	41
1g	(BiFe)-gel-**I**	8.0 [4)]	1 K/min, 650 °C, 1 h	BF + SP (5 wt.%)	70
1h	(BiFe)-gel-**I**	8.0 [4)]	1 K/min, 750 °C, 1 h	BF + SP (38 wt.%)	243
2	(BiFe)-gel-**IA**	1.25 [4)]	1 K/min, 550 °C, 1 h	BF + SP (2 wt.%)	48
3	(BiFe)-gel-**II**	4.8 [5)]	1 K/min, 550 °C, 1 h	BF + SP (16 wt.%)	50
4	(BiFe)-gel-**IIA**	8.0 [5)]	1 K/min, 550 °C, 1 h	BF + SP (11 wt.%)	36

1) C/N = carbon/nitrate ratio
2) BF = $BiFeO_3$; SP = secondary phases (weight proportion)
3) volume-weight-crystallite size of the $BiFeO_3$ phase
4) using acetic acid
5) using nitric acid

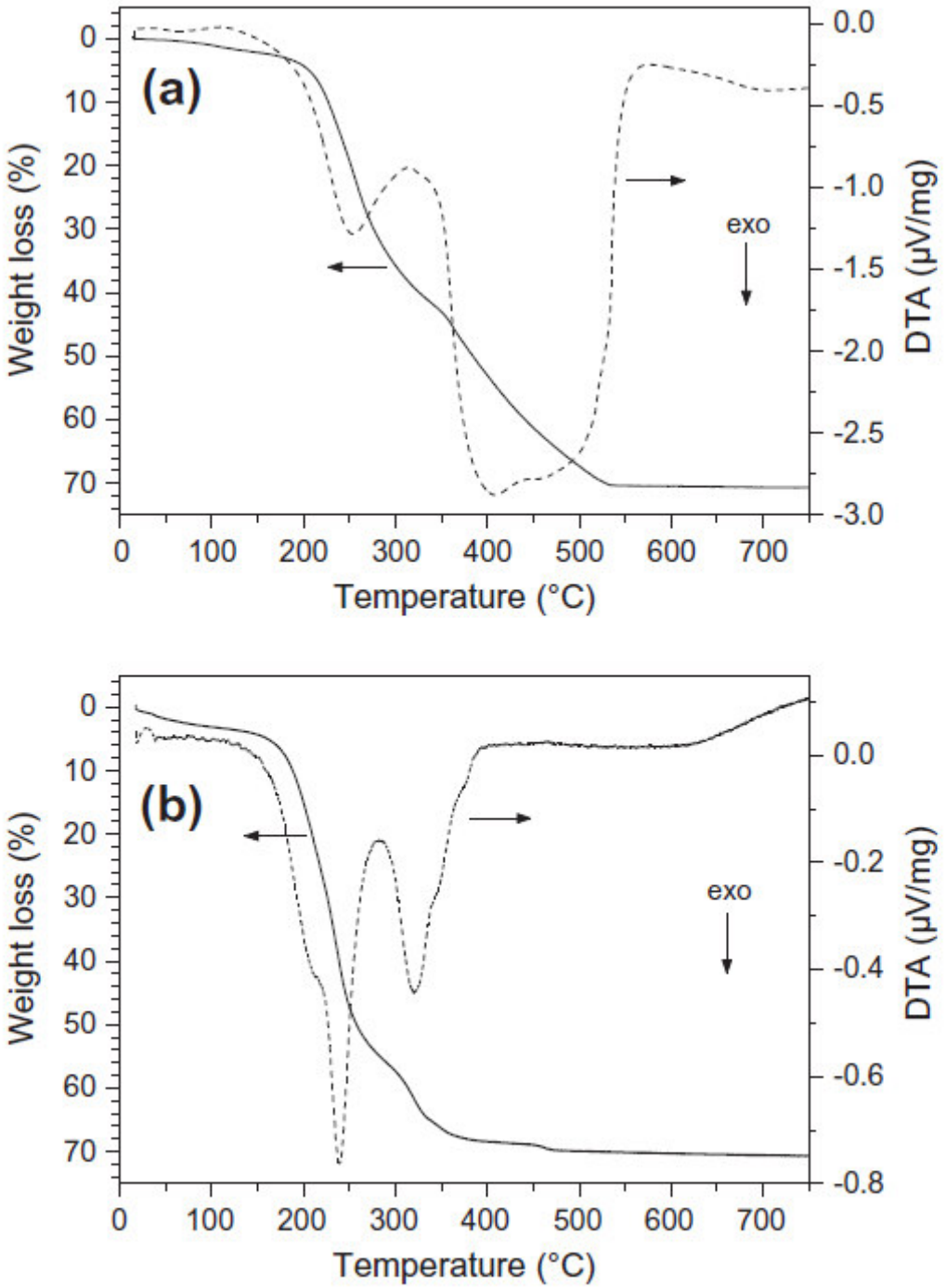

Fig. 1. Simultaneous TG/DTA investigations of the preheated (BiFe)-gel-**I** in flowing air with a heating rate of 10 K/min (a) and 1 K/min (b), respectively.

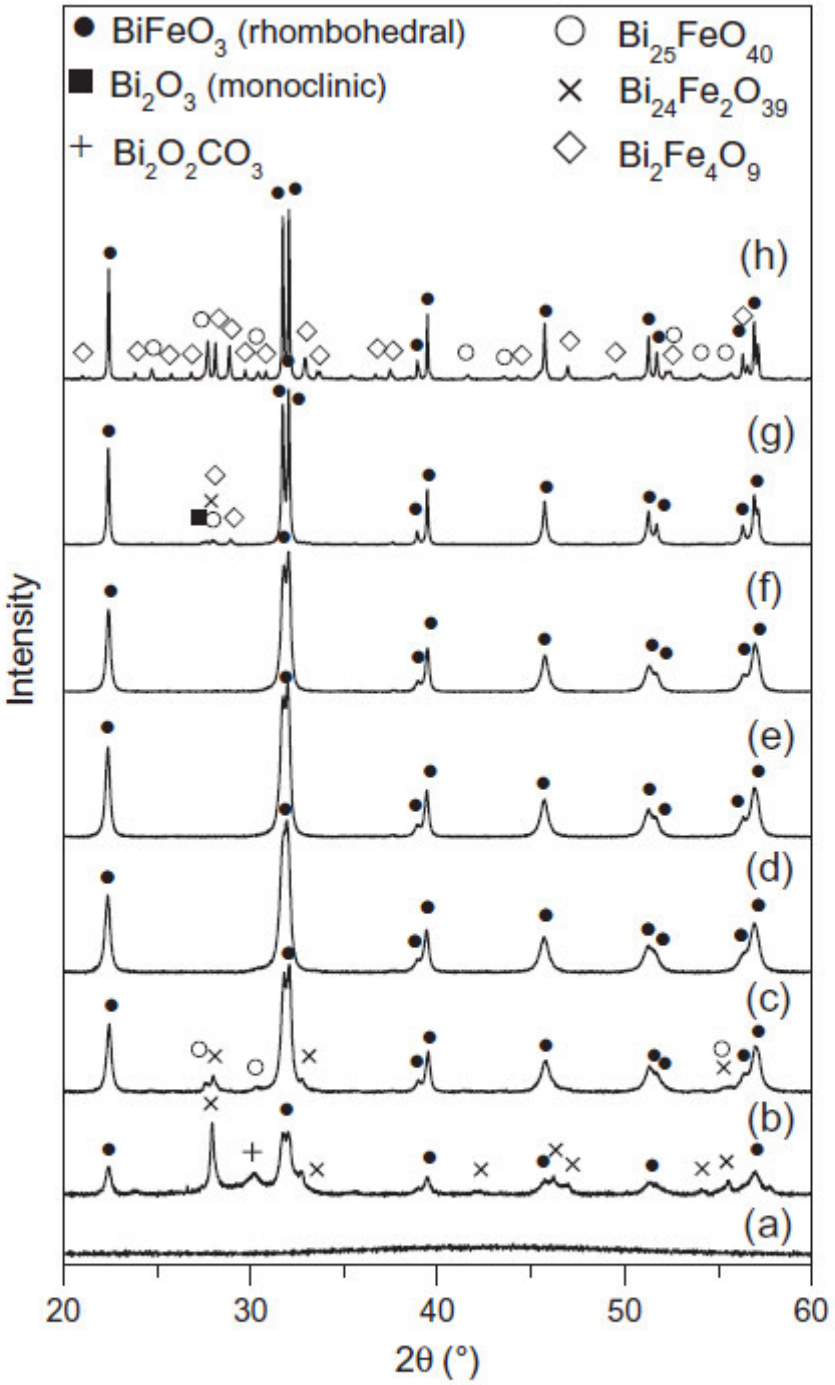

Fig. 2. Room temperature XRD patterns of the (BiFe)-gel-**I** (a) and resulting calcination products (b–h) at various temperatures (heating rate 1 K/min): (b) 400 °C, 1 h, (c) 500 °C, 1 h (powder **1a**), (d) 500 °C, 5 h (powder **1b**), (e) 550 °C, 1 h (powder **1c**), (f) 600 °C, 1 h (powder **1f**), (g) 650 °C, 1 h (powder **1g**), (h) 750 °C, 1 h (powder **1h**).

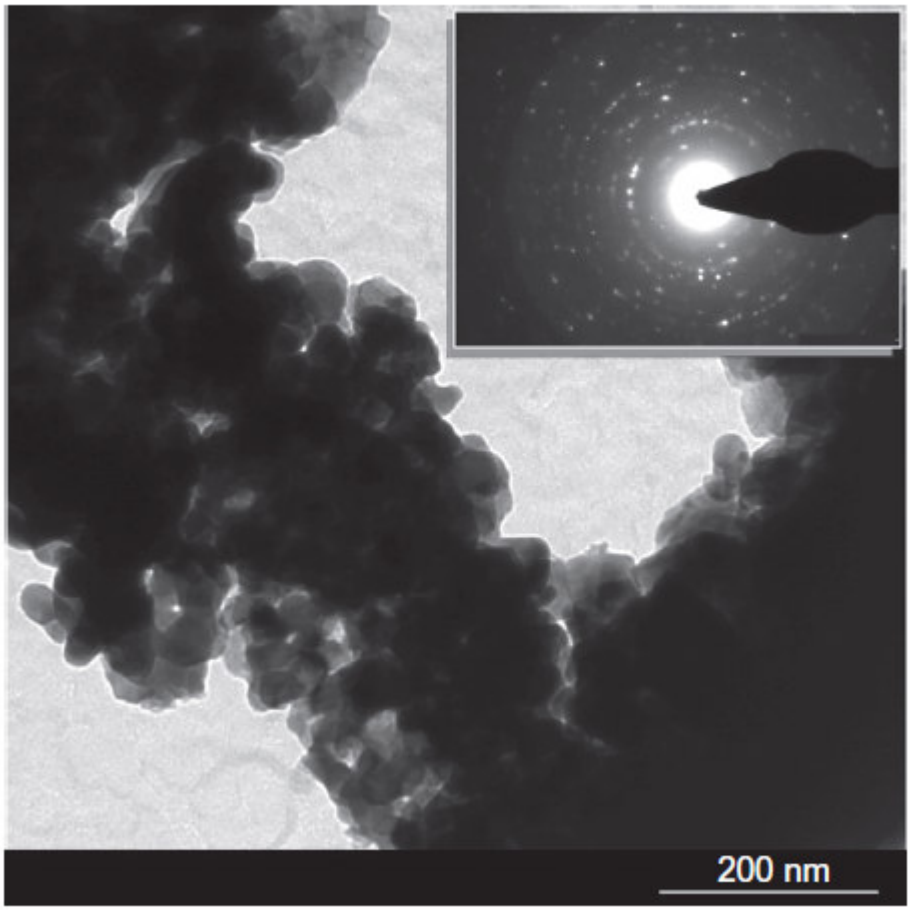

Fig. 3. TEM images of powder **1c**.

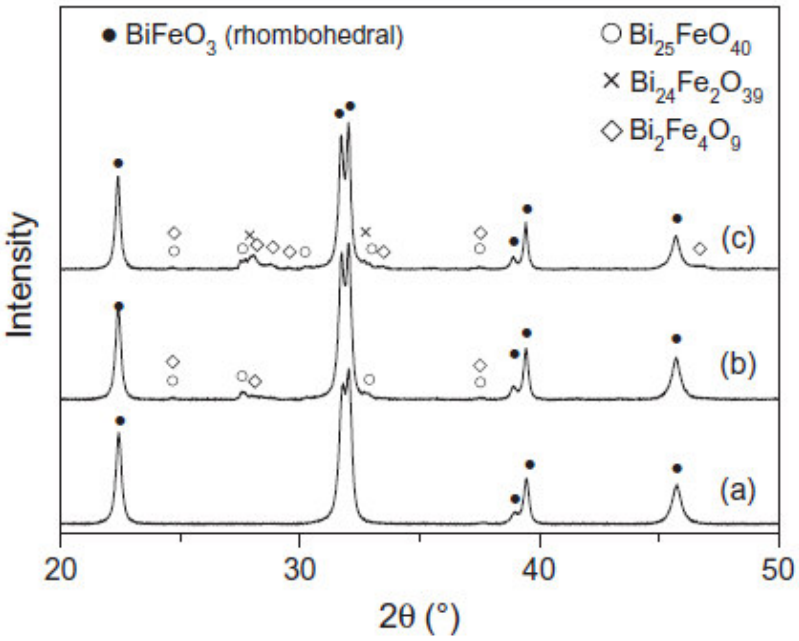

Fig. 4. Room temperature XRD patterns of calcination products of (BiFe)-gel-**I** (b–h) at 550 °C with various heating rates and soaking times. (a) 1 K/min, 4 h, (b) 1 K/min, 5 h (powder **1d**), (c) 10 K/min, 1 h (powder **1e**).

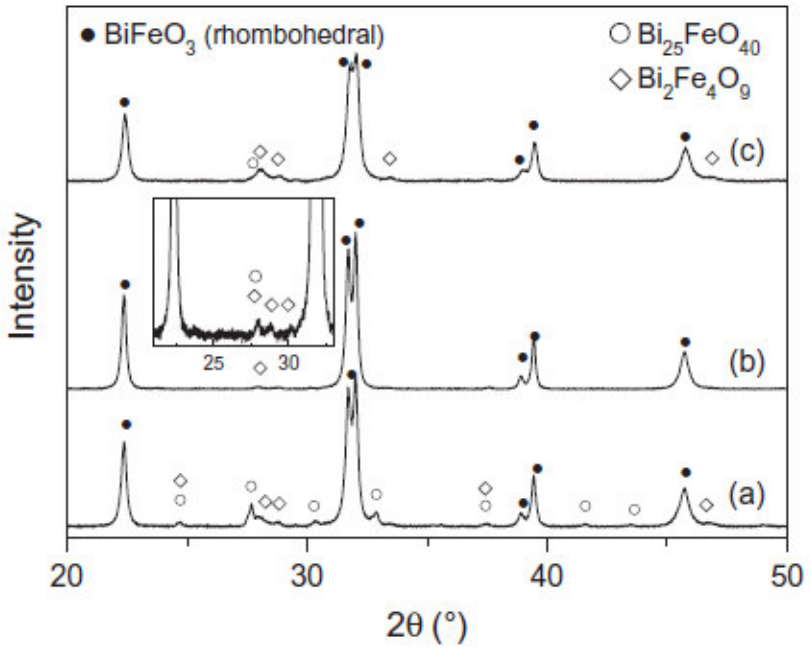

Fig. 5. Room temperature XRD patterns of different (BiFe)-gels calcined at 550 °C for 1 h with a heating rate of 1 K/min. (a) (BiFe)-gel-**IA** (powder **2**), (b) (BiFe)-gel-**II** (powder **3**) and (c) (BiFe)-gel-**IIA** (powder **4**).

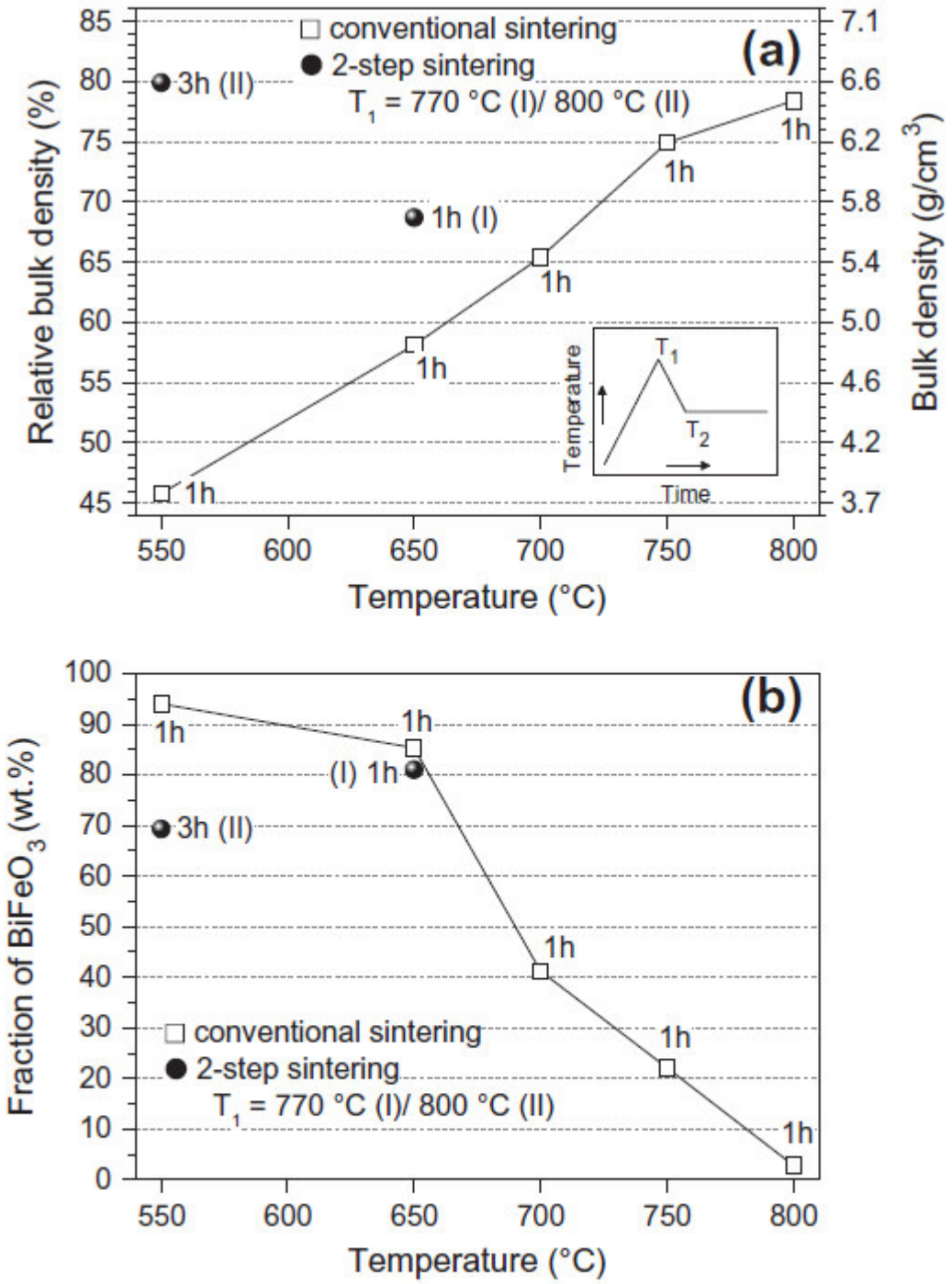

Fig. 6. (a) Final bulk densities versus sintering temperatures at the indicated soaking times of ceramic bodies from powder **1c** after a conventional sintering regime and a 2-step sintering process, respectively. The inset shows a schematic representation of the 2-step sintering process. (b) Decomposition of $BiFeO_3$ during various sintering processes.

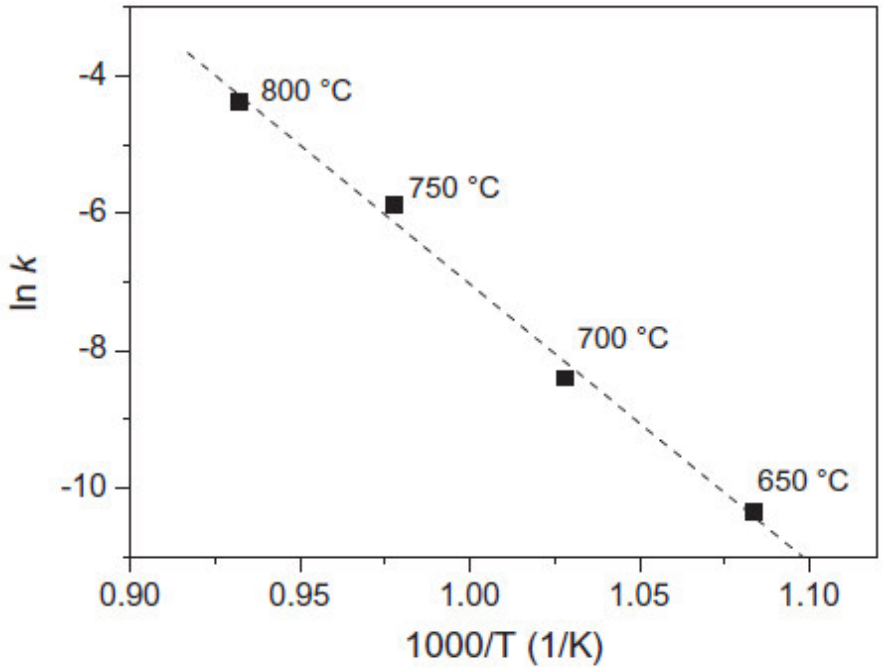

Fig. 7. Arrhenius plot (ln$k$ versus $1/T$) for the decomposition of $BiFeO_3$ compacts from **1c** during conventional sintering.

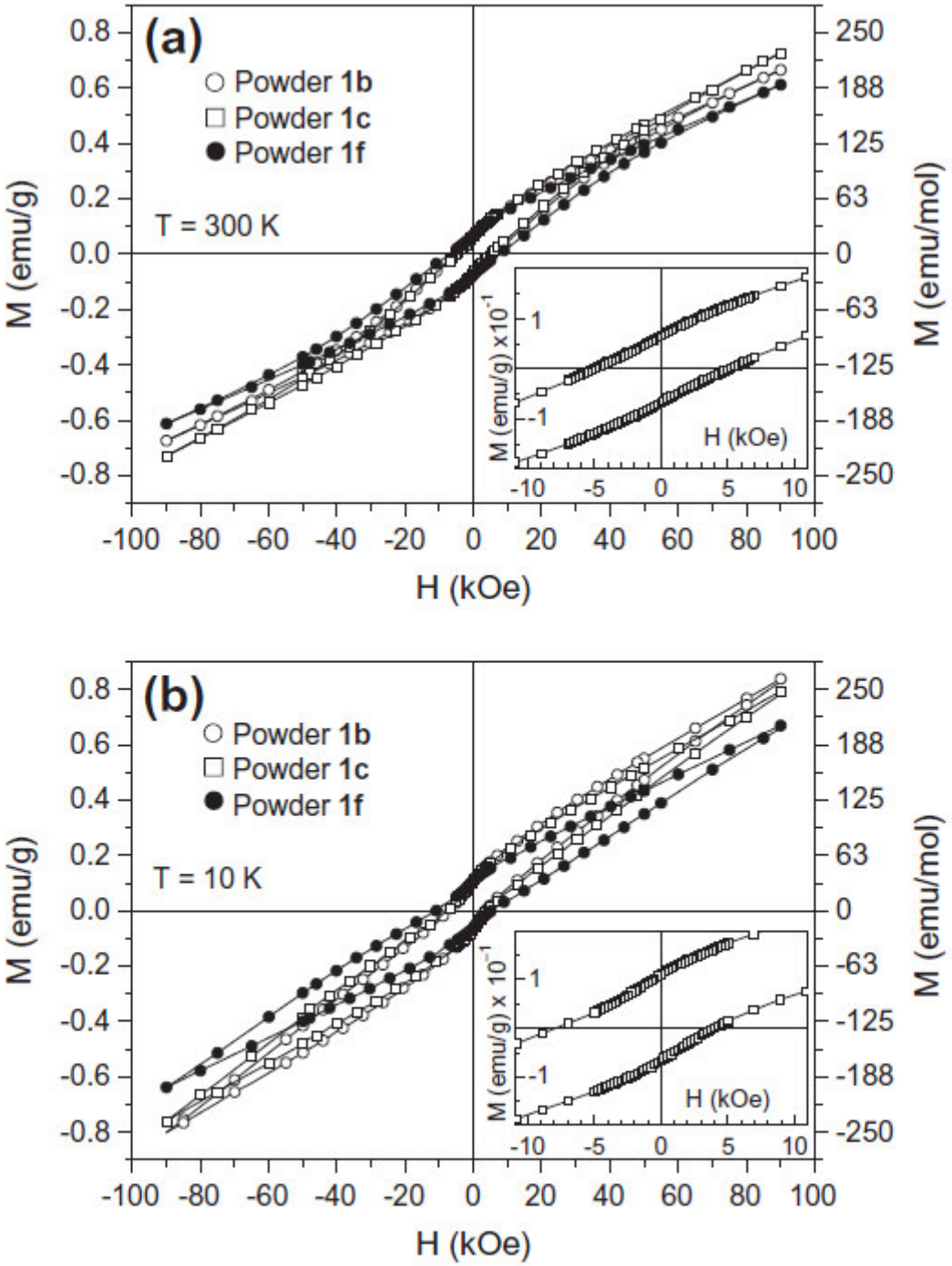

Fig. 8. Magnetization versus applied magnetic field for powders **1b**, **1c** and **1f** at 300 K (a) and 10 K (b), respectively. The insets shows a section between about $H = +11$ and -11 kOe for powder **1c**.

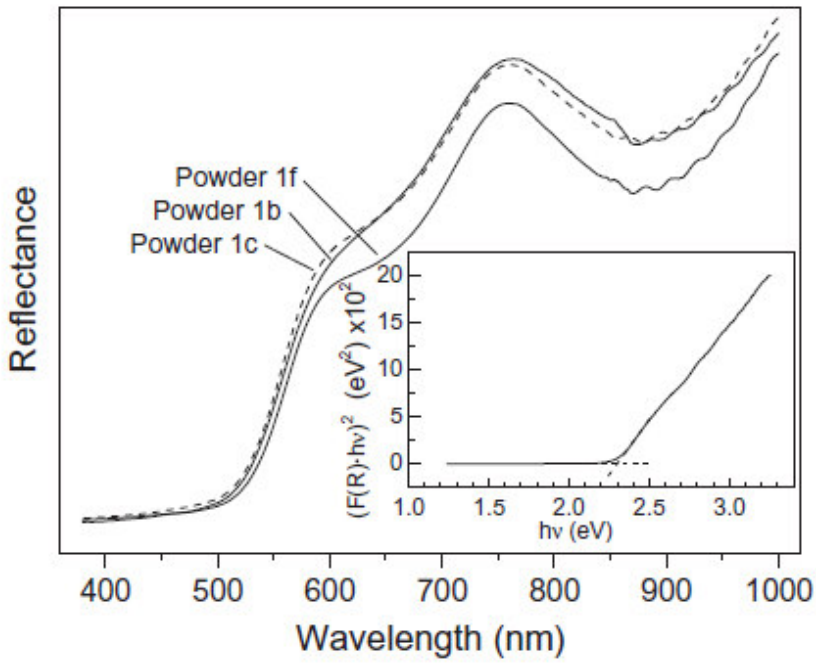

Fig. 9. Diffuse reflectance spectra of powder **1b**, **1c**, and **1f**. The inset shows $(F(R)\cdot h\nu)^2$ versus $h\nu$ of powder **1b**.

References

[1] K. Y. Yun, M. Noda, M. Okuyama, *Appl. Phys. Lett.* 83 (2003) 3981–3983.

[2] Y. Wei, X. Wang, J. Jia, X. Wang, *Ceram. Int.* 38 (2012) 3499–3502.

[3] J.F. Scott, *Nat. Mater.* 6 (2007) 256–257.

[4] Y.-H. Lee, J.-M. Wu, C.-H. Lai, *Appl. Phys. Lett.* 88 (2006) 042903–042905.

[5] X. Wang, Y. Lin, X. Ding, J. Jiang, *J. Alloys Compd.* 509 (2011) 6585–6588.

[6] F. Gao, Y. Yuan, K.F. Wang, X.Y. Chen, F. Chen, J.-M. Liu, Z. F. Ren, *Appl. Phys. Lett.* 89 (2006) 102506.

[7] M. Alexe and D. Hesse, *Nature Commun.* 256 (2011) 1–5.

[8] X.Y. Chen, T. Yu, F. Gao, H.T. Zhang, L.F. Liu, Y.M. Wang, Z.S. Li, Z.G. Zou, *Appl. Phys. Lett.* 91 (2007) 022114.

[9] W. Luo, L. Zhu, N. Wang, H. Tang, M. Cao, Y. She, *Environ. Sci. Technol.* 44 (2010) 1789−1791.

[10] S. Farhadi, M. Zaidi, *J. Mol. Catal. A: Chem.* 299 (2009) 18–25.

[11] I. Sosnowskat, T. Peterlin-Neumaier, E. Steichele, *J. Phys. C: Solid State Phys.* 15 (1982) 4835−4846.

[12] J. Wang, J.B. Neaton, H. Zheng, V. Nagarajan, S.B. Ogale, B. Liu, D. Viehland, V. Vaithyanathan, D.G. Schlom, U.V. Waghmare, N.A. Spaldin, K.M. Rabe, M. Wuttig, R. Ramesh, *Science* 299 (2003) 1719−1722.

[13] D.C. Arnold, K.S. Knight, F.D. Morrison, P. Lightfoot, *Phys. Rev. Lett.* 102 (2009) 027602.

[14] T. Xian, H. Yang, J.F. Dai, Z.Q. Wei, J.Y. Ma, W.J. Feng, *Mater. Lett.* 65 (2011) 1573–1575.

[15] S. Basu, SK.M. Hossain, D. Chakravorty, M. Pal, *Curr. Appl. Phys.* 11 (2011) 976−980.

[16] K. L. Da Silva, D. Menzel, A. Feldhoff, C. Kübel, M. Bruns, A. Paesano Jr., A. Düvel, M. Wilkening, M. Ghafari, H. Hahn, F.J. Litterst, P. Heitjans, K.D. Becker, V. Sepelak, *J. Phys. Chem.* C115 (2011) 7209–7217.

[17] W. Luo, S. Zhang, D. Wang, Y. Ma, F. Wang, K. Watanabe, *J. Magn. Magn. Mater.* 324 (2012) 2458–2462.

[18] S. Vijayanand, M.B. Mahajan, H.S. Potdar, P.A. Joy, *Phys. Rev.* 80 (2009) 064423.

[19] Lei Zhang, X.-F. Cao, Y.-L. Ma, X.-T. Chen, Z.-L. Xue, *J. Solid State Chem.* 183 (2010) 1761–1766.

[20] J. Zou, J. Jiang, Y. Zhang, J. Ma, Q. Wan, *Mater. Lett.* 72 (2012) 134–136.

[21] J. Yang, X. Li, J. Zhou, Y. Tang, Y. Zhang, Y. Li, *J. Alloys Compd.* 509 (2011) 9271–9277.

[22] S. M. Selbach, M.-A. Einarsrud, T. Tybell, T. Grande, *J. Am. Ceram. Soc.* 90 (2007) 3430–3434.

[23] M.C. Navarro, M.C. Lagarrigue, J.M. De Paoli, R.E. Carbonio, M.I. Gomez, *J. Therm. Anal. Calorim.* 16602 (2010) 655–660.

[24] A. Hardy, S. Gielis, H. Van den Rul, J. D'Haen, M.K. Van Bael, J. Mullens, *J. Eur. Ceram. Soc.* 29 (2009) 3007–3013.

[25] V. Kothai and R. Ranjan, *Bull. Mater. Sci.* 35 (2012) 157−161.

[26] F. Gao, X. Chen, K. Yin, S. Dong, Z. Ren, F. Yuan, T. Yu, Z. Zou, J.-M. Liu, *Adv. Mater.* 19 (2007) 2889–2892.

[27] V. Fruth, L. Mitoseriu, D. Berger, A. Ianculescu, C. Matei, S. Preda, M. Zaharescu, *Prog. Solid State Chem.* 35 (2007) 193−202.

[28] C. Madhu, M.B. Bellakki, V. Manivannan, *Ind. J. Eng. Mater.* 17 (2010) 131−139.

[29] M.B. Bellakki, V. Manivannan, C. Madhu, A. Sundaresan, *Mater. Chem. Phys.* 116 (2009) 599–602.

[30] X. Wu, W. Wu, X. Cui, S. Liao, *J. Thermal. Anal. Calorim.* 107 (2012) 625−632.

[31] Y.R. Dai,Q. Xu, X. Zheng, S. Yuan, Y.Zhai, M. Xu, *Physica* B407 (2012) 560–563.

[32] Q. Xu, X. Zheng, Z. Wen, Y. Yang, D. Wu, M. Xu, *Solid State Comm.* 151 (2011) 624−627.

[33] J.K. Kim, S.S. Kim, W.-J. Kim, *Mater. Lett.* 59 (2005) 4006–4009.

[34] M. Mahesh Kumar, V.R. Palkar, K. Srinivas, S.V. Suryanarayana, *Appl. Phys. Lett.* 76 (2000) 2764−2766.

[35] R. Mazumder, P. Sujatha Devi, D. Bhattacharya, P. Choudhury, A. Sen, M. Raja, *Appl. Phys. Lett.* 91 (2007) 062510.

[36] M. Arora, P.C. Sati, S. Chauhan, S. Chhoker, A.K. Panwar, M. Kumar, *J. Supercond. Nov. Magn.* 26 (2013) 443–448.

[37] J. Deng, S. Banerjee, S.K. Mohapatra, Y.R. Smith, M. Misra, *Journal of Fundamentals of Renewable Energy and Applications*, 1 (2011) R101204.

[38] S.F. Radaev, L.A. Muradyan, V.I. Simonov, Acta Cryst. B47 (1991) 1–6.

[39] D.C. Craig and N.C. Stephenson, *J. Solid State Chem.* 15 (1975) 1–8.

[40] S. Phapale, R. Mishra, D. Das, *J. Nucl. Mater.* 373 (2008) 137–141.

[41] S.M. Selbach, M.-A. Einarsrud, T. Grande, *Chem. Mater.* 21 (2009) 169–173.

[42] J. Lu, L.J. Qiao, P.Z. Fu, Y.C. Wu, *J. Cryst. Growth* 318 (2011) 936–941.

[43] X. Liu, X. Dou, H.Y. Xie, J.-F. Chen, *Key Eng. Mater.* 512–515 (2012) 1235–1239.

[44] R. Haumont, I.A. Kornev, S. Lisenkov, L. Bellaiche, J. Kreisel, B. Dkhil, *Phys. Rev.* B78 (2008) 134108.

[45] R. Palai, R.S. Katiyar, H. Schmid, P. Tissot, S.J. Clark, J. Robertson, S.A.T. Redfern, G. Catalan, J.F. Scott, *Phys. Rev.* B77 (2008) 014110.

[46] R. Köferstein, D. Hesse, S.G. Ebbinghaus, *Solid State Ionics* 203 (2011) 52–56.

[47] R. Köferstein and S.G. Ebbinghaus, *Solid State Ionics* 231 (2013) 43–48.

[48] J. Rodriguez-Carvajal, *Physica* B192 (1993) 55–69.

[49] W. Kraus and G. Nolze, *Powder Diffr.* 13 (1998) 256–259.

[50] Program WinXPOW v1.06, Stoe & Cie GmbH, Darmstadt (1999).

[51] A.R. Stokes, and A.J.C. Wilson, *Proc. Phys. Soc.* 56 (1944) 174–181.

[52] PDF 2 (International Centre for Diffraction Data, Pennsylvania) 2001, $BiFeO_3$ [71-2494], Fe_2O_3 [85-599], $Bi_{24}Fe_2O_{39}$ [42-201], $Bi_{25}FeO_{40}$ [46-416], $Bi_2Fe_4O_9$ [74-1098], $Bi_2O_{3\ (monoclinic)}$ [71-465], $Bi_2O_2CO_3$ [84-1752].

[53] W. Chen, A.J. Williams, L. Ortega-San-Martin, M. Li, D.C. Sinclair, W. Zhou, J.Paul Attfield, *Chem. Mater.* 21 (2009) 2085–2093.

[54] T.T. Carvalho and P.B. Tavares, *Mater. Lett.* 62 (2008) 3984–3986.

[55] M.I. Morozov, N.A. Lomanova, V.V. Gusaroven, *Russ. J. Gen. Chem.* 73 (2003) 1772−1776.

[56] M.N. Deraz, *J. Alloys Compd.* 501 (2010) 317–325.

[57] C.C. Hwang and T.Y. Wu, *Mater. Sci. Eng.* B111 (2004) 197–206.

[58] K. Deshpande, A. Mukasyan, A. Varma, *Chem. Mater.* 16 (2004) 4896–4904.

[59] V.M. Khot, A.B. Salunkhe, M.R. Phadatare, S.H. Pawar, *Mater. Chem. Phys.* 132 (2012) 782–787.

[60] C.C. Mardare, P.B. Tavares, A.I. Mardare, R. Savu, *Mater. Sci. Forum* 514−516 (2006) 328−332.

[61] J. Rymarczyk, D. Machura, J. Ilczuk, *Eur. Phys. J. Special Topics* 154 (2008) 191–194.

[62] J.M. Moreau, C. Michel, R. Gerson, W.J. James, *J. Phys. Chem. Solids* 32 (1971) 1315−1320.

[63] J. Huberty and H. Xu, *J. Solid State Chem.* 181 (2008) 508–514.

[64] J. Graetz and J.J. Reilly, *J. Phys. Chem.* B109 (2005) 22181−22185.

[65] R. Köferstein, L. Jäger, M. Zenkner, H.-P. Abicht, *J. Mater. Sci.* 43 (2008) 832−838.

[66] Y.P. Wang, L. Zhou, M.F. Zhang, X.Y. Chen, J.M. Liu, Z.G. Liu, *Appl. Phys. Lett.* 84 (2004) 1731−1733.

[67] S. Chikazumi, Physics of Ferromagnetism, second ed., Oxford University Press Inc., New York, 1997.

[68] L. Néel, *Rev. Mod. Phys.* 25 (1953) 58−63.

[69] T. Moriya, *Phys. Rev.* 120 (1960) 91−98.

[70] B. Bhushan, Z. Wang, J. van Tol, N.S. Dalal, A. Basumallick, N.Y. Vasanthacharya, S. Kumar,D. Das, *J. Am. Ceram. Soc.* (2012) 1−8.

[71] T.-J. Park, G.C. Papaefthymiou, A.J. Viescas, A.R. Moodenbaugh, S.S. Wong, *Nano Lett.* 7 (2007) 766−772.

[72] P. Kubelka and F. Munk, *Z. Techn. Phys.* 11 (1931) 593−601.

[73] G. Kortüm and J. Vogel, *Z. Phys. Chem.* 18 (1958) 110−122.

[74] S.M. Sze, Physics of Semiconductor Devices, J. Wiley & Sons, 1969, p. 52.

[75] T.P McLean, in: A.F. Gibson (Ed.), Progress in Semiconductors, Vol. 5, 1960, pp. 55−102.

[76] O. Schevciw and W. B. White, *Mater. Res. Bull.* 18 (1983) 1059−1068.

[77] S. Li, Y.-H. Lin, B.-P. Zhang, Y. Wang, C.-W. Nan, *J. Phys. Chem.* C114 (2010) 2903–2908.

[78] S.R. Basu, L.W. Martin, Y.H. Chu, M. Gajek, R. Ramesh, R.C. Rai, X. Xu, J.L. Musfeldt, *Appl. Phys. Lett.* 92 (2008) 091905.

[79] G. Catalan and J.F. Scott, *Adv. Mater.* 21 (2009) 2463–2485.